Geophysical Journal International

Geophys. J. Int. (2016) **205,** 785–795 doi: 10.1093/gji/ggw036

GJI Marine geosciences and applied geophysics

Ice shelf structure derived from dispersion curve analysis of ambient seismic noise, Ross Ice Shelf, Antarctica

A. Diez,[1] P.D. Bromirski,[1] P. Gerstoft,[1] R.A. Stephen,[2] R.E. Anthony,[3] R.C. Aster,[3] C. Cai,[4] A. Nyblade[5] and D.A. Wiens[4]

[1] *Scripps Institution of Oceanography, University of California, San Diego, La Jolla, CA* 92093-0209, *USA. E-mail: adiez@ucsd.edu*
[2] *Woods Hole Oceanographic Institution, Woods Hole, MA* 02543, *USA*
[3] *Department of Geosciences, Warner College of Natural Resources, Colorado State University, Fort Collins, CO* 80523-1482, *USA*
[4] *Department of Earth and Planetary Sciences, Washington University in St. Louis, St. Louis, MO* 63130-4899, *USA*
[5] *Department of Geosciences, Pennsylvania State University, State College, PA* 16801, *USA*

Accepted 2016 January 20. Received 2016 January 6; in original form 2015 September 5

SUMMARY

An L-configured, three-component short period seismic array was deployed on the Ross Ice Shelf, Antarctica during November 2014. Polarization analysis of ambient noise data from these stations shows linearly polarized waves for frequency bands between 0.2 and 2 Hz. A spectral peak at about 1.6 Hz is interpreted as the resonance frequency of the water column and is used to estimate the water layer thickness below the ice shelf. The frequency band from 4 to 18 Hz is dominated by Rayleigh and Love waves propagating from the north that, based on daily temporal variations, we conclude were generated by field camp activity. Frequency–slowness plots were calculated using beamforming. Resulting Love and Rayleigh wave dispersion curves were inverted for the shear wave velocity profile within the firn and ice to ∼150 m depth. The derived density profile allows estimation of the pore close-off depth and the firn–air content thickness. Separate inversions of Rayleigh and Love wave dispersion curves give different shear wave velocity profiles within the firn. We attribute this difference to an effective anisotropy due to fine layering. The layered structure of firn, ice, water and the seafloor results in a characteristic dispersion curve below 7 Hz. Forward modelling the observed Rayleigh wave dispersion curves using representative firn, ice, water and sediment structures indicates that Rayleigh waves are observed when wavelengths are long enough to span the distance from the ice shelf surface to the seafloor. The forward modelling shows that analysis of seismic data from an ice shelf provides the possibility of resolving ice shelf thickness, water column thickness and the physical properties of the ice shelf and underlying seafloor using passive-source seismic data.

Key words: Glaciology; Surface waves and free oscillations; Seismic anisotropy; Antarctica.

1 INTRODUCTION

Iceberg calving and basal melting of ice shelves accounts for the largest amount of Antarctica's ice mass losses (Pritchard *et al.* 2012). Although melting of ice shelves does not contribute to sea level rise, they are important because they restrain the discharge of contributing glaciers into the oceans (Dupont & Alley 2005). Loss of ice shelf mass and/or ice shelf strength reduces the buttressing effect, leads to speedup of glaciers, a faster discharge of previously grounded ice and, thus, an acceleration of sea-level rise (Rignot *et al.* 2004). Hence, considerable effort has been made to determine the mass budget and physical properties of ice shelves, primarily using remote sensing techniques.

Critical here is the understanding of the factors that lead to calving events of large tabular icebergs or the collapse of ice shelves, as occurred at the Larsen A (1995), Larsen B (2002; Rack & Rott 2004) and Wilkins (2008; Braun *et al.* 2009) ice shelves. Possible factors that may lead to ice shelf fragmentation include melt pond formation and associated water penetration into crevasses (Scambos *et al.* 2009; Banwell *et al.* 2013) and fracturing process of rifts (Bassis *et al.* 2007; Jansen *et al.* 2015). Other studies note the influence of the ocean–ice shelf interactions, that is, processes influencing basal melting (Liu *et al.* 2015) and the impact of ocean waves on ice shelves (Bromirski *et al.* 2010).

The integrity of firn on an ice shelf can be estimated from the firn–air content thickness (Holland *et al.* 2011; Kuipers Munneke *et al.* 2014), that is, the pore space fraction over the firn column

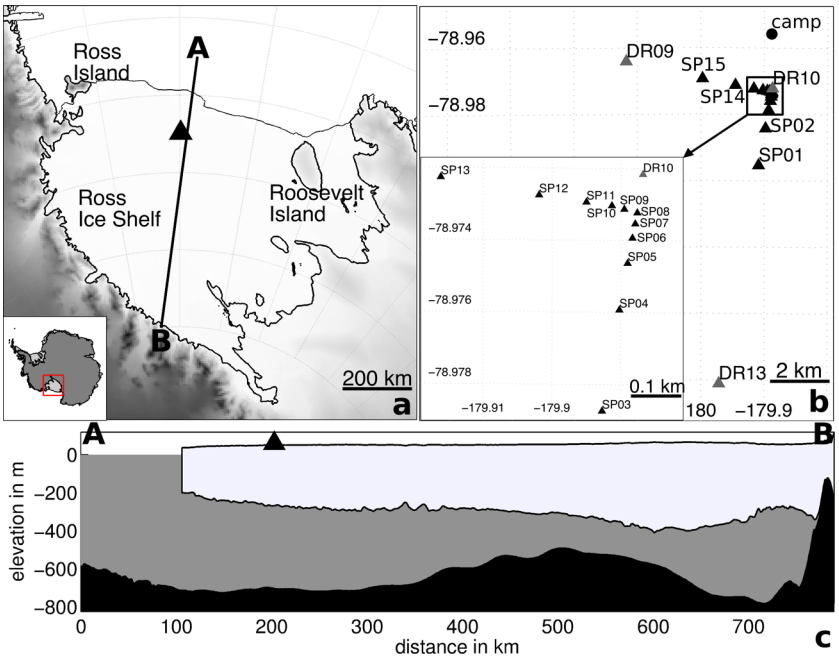

Figure 1. (a) Location of the short-period (SP) array (black triangle) on the Ross Ice Shelf, Antarctica (inset). (b) Overview of station locations in the survey area on the Ross Ice Shelf, with the inset showing an expanded view of the station configuration at the centre of the survey area. (c) Cross-section produced from Bedmap2 data (Fretwell *et al.* 2013) showing ice and water layer thickness along a transect from the ice front to the grounding zone parallel to the survey line from SP01 to SP08 (black line in panel a).

given as a corresponding thickness. Increasing temperatures and/or melting and refreezing processes result in increased densification of the firn and cause the reduction of the firn-air content thickness. On the other hand, an increase in snow accumulation can lead to an increase in firn-air content thickness (Ligtenberg *et al.* 2014).

Most measurements and observations of ice shelves are based on satellite data (e.g. Pritchard *et al.* 2012; Rignot *et al.* 2013; Depoorter *et al.* 2013; Paolo *et al.* 2015). Much sparser on-ice measurements include global positioning system (GPS) measurements (e.g. Vaughan 1994; King *et al.* 2000) or radar measurements (Corr *et al.* 2002; Drews 2015) and a few seismic studies (Fricker *et al.* 2005; Brisbourne *et al.* 2014; Zhan *et al.* 2014; Eisen *et al.* 2015). All of these studies are typically conducted over limited time periods during the austral summer. Here we study passive-source data collected by a seismometer array on the Ross Ice Shelf for 11 days to determine local ice shelf structure.

The Ross Ice Shelf is Earth's largest ice shelf with an area of about 492 000 km^2 (Depoorter *et al.* 2013). Six ice streams (Mercer, Whillans, Kamb, Bindschadler, MacAyeal and Echelmeyer) discharge ice to the Ross Ice Shelf. Direct measurements of the Ross Ice Shelf are limited, particularly during the austral winter. The most comprehensive studies on the Ross Ice Shelf were done within the RIGGS project (Bentley 1990), that included numerous gridded geophysical and glaciological measurements conducted between 1973 and 1978. More recent studies have focused on the surrounding glaciers, especially the Whillans Ice Stream, where several seismic, radar, GPS and borehole measurements were carried out (e.g. Christianson *et al.* 2012; Horgan *et al.* 2012, 2013; Pratt *et al.* 2014).

We study ambient–noise seismic data from the Ross Ice Shelf, from stations located about 100 km landwards of the ice shelf front. Using array analysis, we show that a significant amount of seismic energy is locally generated and propagates as surface waves from the north. The corresponding Love and Rayleigh wave dispersion curves are inverted to estimate the *S*-wave velocity structure of the Ross Ice Shelf at this location. To investigate the effect of a water interlayer on the dispersion curve characteristics, we model surface wave dispersion curves for firn/ice/water/seafloor layered structures constrained by the *S*-wave velocity profile.

2 DATA

An array of 34 broadband (BB) seismometers (fig. 1, Bromirski *et al.* 2015) was installed on the Ross Ice Shelf in November 2014 to continuously record a variety of seismic signals on the ice shelf, including gravity wave-induced vibrations and teleseismic waveforms, for 2 yr. An additional array of 15 short-period (SP) three-component Sercel L22 seismometers (eigenfrequency of 2 Hz) was installed at the beginning of this deployment campaign. All SP seismometers were buried at a depth of about 0.2 m. The SP array is nested at the centre of the BB array, and the arms of the SP array are colinear with the BB array arms. The SP array collected data for 11 days from 18 to 29 November 2014. The array was configured in an L-shape with logarithmic-periodic intersensor spacing between the seismometers (Fig. 1). The corner of the array, station SP08, was located at S78° 58′24.227, W179° 53′15.374 at the beginning of recording on 16 November 2014, drifting northwards at approximately 3 m d^{-1} due to ice shelf movement. Additionally, data from three BB stations (DR09, DR10 and DR13), in the vicinity of the SP array, were collected at the close of deployment operations (Fig. 1b), that is, data were recorded over a time period of 5–12 days, depending on the time of station installation. The data were sampled at 200 Hz for both the SP and BB arrays, except data of station SP08, which were sampled at 500 Hz and are not used in this study. All

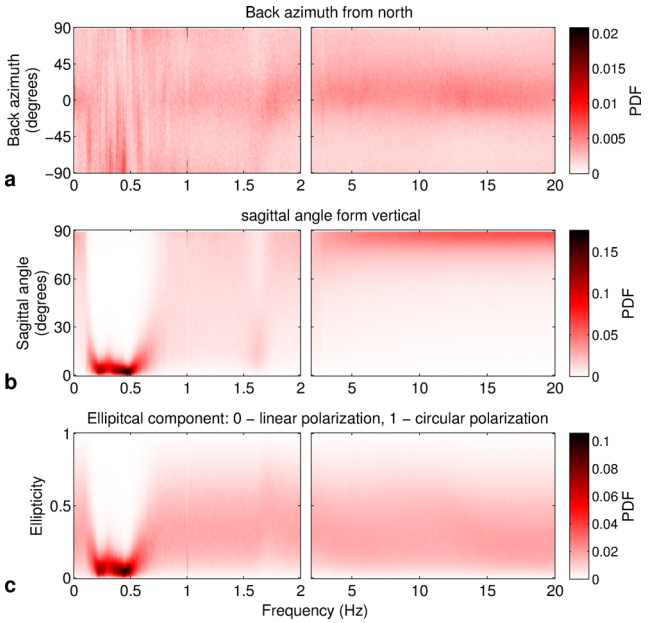

Figure 2. Empirical probability density functions (PDF) averaged over all SP stations of polarization attributes: (a) backazimuth, (b) sagittal angle, and (c) ellipticity derived from the SP data collected during 18–29 November 2014.

data studied are presented here as velocity response (m s^{-1}) and are corrected for their instrument response.

3 POLARIZATION ANALYSIS

Polarization analyses (e.g. Koper & Hawley 2010; Riahi *et al.* 2013) of the SP data for the complete time interval were undertaken to determine ambient noise propagation characteristics in the ice. We determined the polarization attributes, backazimuth, sagittal angle and ellipticity, over 0–20 Hz from the three-component data for each station following the methodologies of Vidale (1986) and Jurkevics (1988). The frequency (f) dependent complex spectrum, $y(f)$, was calculated from 10 min data segments for all three components (V: vertical, N: north, E: east), resulting in a frequency resolution of 0.0017 Hz. The spectral density matrix S was then calculated for each time segment by multiplying the complex spectra $y(f)$ by its Hermitian transpose $y^*(f)$:

$$S_{jk} = y_j(f)y_k^*(f), \tag{1}$$

with j, k = V, N, E. Subsequently, six 10 min spectral density matrices were averaged, and eigenvalues and eigenvectors were calculated from this averaged spectral density matrix. Polarization attributes were calculated from the largest eigenvalue and corresponding eigenvector (Vidale 1986; Jurkevics 1988). The backazimuth is given relative to north. The sagittal angle is the angle measured from vertical within the vertical–backazimuth plane. The ellipticity spans the range from linear polarization (0) to circular polarization (1).

To analyse the frequency dependence of the polarization attributes, we determined the empirical probability density function (PDF) for each attribute for each station over the full data record. Single-station PDFs are very similar, justifying the averaging of PDFs of all SP stations to identify coherent signals common to all stations, resulting in the PDFs shown in Fig. 2. These SP data do not allow resolution of signals below ∼0.2 Hz due to the response characteristics of the L22 seismometers.

Linear polarized waves (ellipticity near zero) with sagittal angle ∼0° are observed between 0.2 and 0.5 Hz (Fig. 2). From 0.5–1.6 Hz, no clear pattern in the sagittal angle is visible, while a backazimuth of 0° (north) and elliptical motion are weakly indicated. An apparent signal is observed at 1.6 Hz, very narrow band and primarily identifiable from its consistent sagittal angle (∼0°). For frequencies above 2 Hz, the sagittal angle exhibits a clustering near 90° and a tendency for propagation from ∼0° backazimuth, indicating horizontal wave propagation from the north. There is some indication of elliptical motion in this band as well, with a concentration of ellipticity spanning about 0.05 to 0.8. Hence, the polarization attributes indicate surface wave propagation above 2 Hz.

4 DISPERSION CURVES

Surface wave dispersion curves from active source seismic data have been used previously to investigate the firn structure by inverting for the shear (S)-wave velocity profile at, for example, Subglacial Lake Whillans, Antarctica (Picotti *et al.* 2015) and the Italian Alps (Godio & Rege 2015). Here, we beamform the passive-source SP seismic array data to obtain the main propagation direction of the surface waves. Inversion of the resulting dispersion curves from that backazimuth allows estimation of firn properties and structure.

4.1 Beamforming to estimate source azimuth

Consistent polarization attributes above 2 Hz (Fig. 2) motivate more detailed investigation of this band with beamforming (Fig. 3). Due to the spacing of the seismometer array, it was not possible to analyse the consistent polarization attributes below 2 Hz with beamforming because the wavelengths below 2 Hz are too long (Fig. 4a). However, the array geometry allows resolution and localization of higher frequency signals (Fig. 4). The source direction of the ambient noise signal was determined by beamforming (Gerstoft & Tanimoto 2007) of the vertical component of the SP array from 2–20 Hz. Beamforming was performed for 10 min data segments, for a slowness range of 0.1–1.2 s km^{-1}, and over azimuths from 0° to 360°. Fig. 3 shows beamforming results for the frequency bins (bin width 0.34 Hz) centred at 2.34, 5.08, 10.16 and 15.23 Hz, averaging all (144) 10 min data segments on 27 November.

For the lowest frequency band analysed (2.34 Hz, Fig. 3), a peak is observed at a backazimuth ∼10° from the north, with an apparent slowness (inverse of the apparent phase velocity) of about 0.5 s km^{-1}. This weak peak occurs along the north-south axis of the array (SP01–SP07; Fig. 1b), and is not as well resolved as the peaks observed at higher frequencies. Between 5 and 15 Hz, a distinct signal from the north is detected, consistent with results from the polarization analysis (Fig. 2a). The signal has an apparent slowness of 0.5–0.7 s km^{-1} (i.e. 1250–2000 m s^{-1}), with an increase in the apparent slowness with frequency.

4.2 Dispersion curves from the north

The distinct signal from the north above 5 Hz motivates a frequency–slowness analysis using only north-south oriented stations SP01–SP07, as this part of the array is nearly inline with the incoming signal. Beamforming results over backazimuths between −20° and 20° from the north were averaged. The frequency–slowness dependency was calculated for all 10 min data segments (frequency bin width

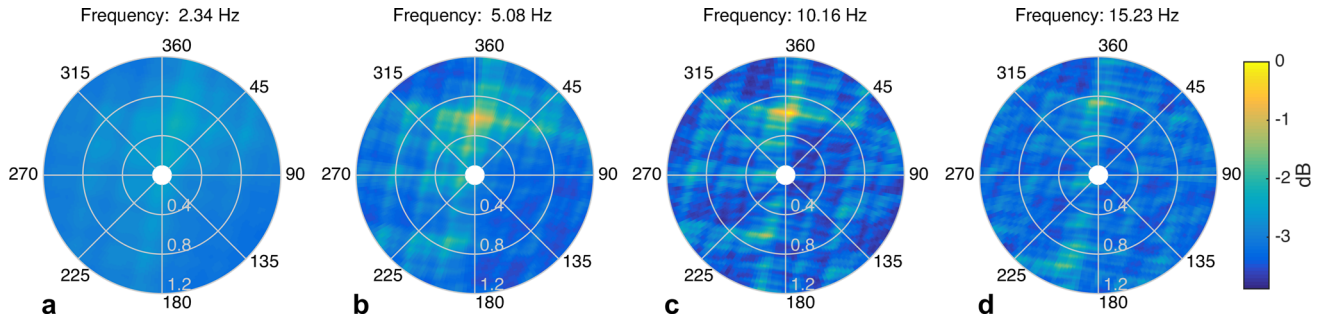

Figure 3. Beamforming of the vertical component (Stations SP01–SP07, SP09–SP15) for frequencies (a) 2.34, (b) 5.08, (c) 10.16 and (d) 15.23 Hz, backazimuths from 0° to 360° (360° - north), and slownesses from 0.1 to 1.2 s km^{-1}. The maxima occur at a backazimuth from the north (∼360°) at slowness of 0.5–0.7 s km^{-1}. The energy is normalized to the global maximum between 2 and 20 Hz.

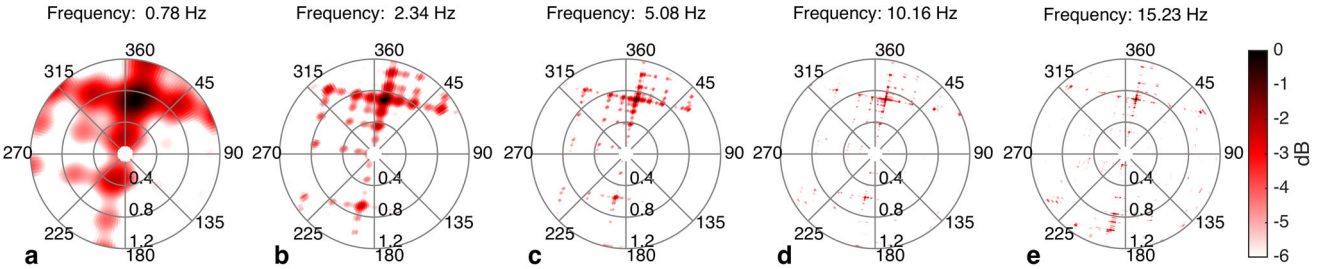

Figure 4. Beampattern of the SP array (Stations SP01-SP07, SP09-SP15) for (a) 0.78, (b) 2.34, (c) 5.08, (d) 10.16 and (e) 15.23 Hz for a wave coming from 10° with 0.7 s km^{-1}. Panel (a) shows insufficient resolution of long wavelengths at frequencies below 2 Hz. The resolution increases with increasing frequency, such that the maximum is detected with less ambiguity, although aliasing effects increase. Sideloops are visible in array axes direction.

0.195 Hz) between 19 and 28 November 2014. Distinct dispersion curves are observed only in some 10 min data segments. Fig. 5(g) shows the occurrence of distinct dispersion curves (black) during the time intervals. Due to the lack of distinct dispersion curves observed between 21 and 25 November, we stacked all 10 min data segments with frequently occurring, distinct dispersion curves over 26–28 November (Fig. 5g) to obtain a representative dispersion curve. Fig. 5 shows the slowness–frequency spectra for the vertical (ZZ, Fig. 5a), the north (NN, Fig. 5b) and the east (EE, Fig. 5c) component.

Dispersion curves can be resolved for all three components between 4 and 18 Hz with apparent slownesses of 0.5–0.8 s km^{-1}, corresponding to the observed peaks in the beamforming (Fig. 3). For the vertical and north components, the dispersion curves follow similar trends, with an energy peak between 4.5 and 6 Hz and apparent slownesses of 0.54–0.64 s km^{-1}. The energy levels are significantly weaker between 5.9 and 6.6 Hz, and increase at higher frequencies. The observed dispersion curve on the east component has lower apparent slownesses below 12.5 Hz compared to the vertical and north components, and higher slownesses above. For the east component, the energy is weaker below 7.2 Hz. In contrast to the vertical and north components, the energy does not increase again below 6 Hz.

Since the observed backazimuth is from the north (Figs 2a and 3), we interpret the dispersion curves on the vertical and north component as Rayleigh wave (coupled compressional (*P*) and vertical shear (*SV*) wave). The dispersion curve on the east component is interpreted as Love wave (horizontal shear (*SH*) wave).

The picked representative dispersion curves for the vertical, north and east components were determined from the maxima of the fundamental mode of the Rayleigh and Love waves within the frequency-slowness domain shown in Figs 5(a)–(c). The maxima were picked for each 10 min time segment considered during 26–28 November (Fig. 5g, black regions), excluding obvious outliers. Displayed in Fig. 5 are the average (dots) and symmetric standard derivation (error bars) calculated from the picked values for the different time segments. The error bars are small: near ±0.005 s km^{-1} for low slownesses, increasing with slowness up to ±0.023 s km^{-1} on the east component. We use the picked dispersion curve values as input for an inversion of the *S*-wave velocity profile.

4.3 Velocity–depth profile from surface wave inversion

S-wave velocity–depth profiles were obtained from inversion of the dispersion curves in Figs 5(a)–(c) using Geopsy (Wathelet *et al.* 2004; Wathelet 2008). The Geopsy forward modelling code (Wathelet *et al.* 2004) solves the associated eigenvalue problem for Love and Rayleigh waves (Dunkin 1965). The inversion is based on a neighbourhood algorithm (Wathelet 2008), using a direct search of the parameter space across a specified range for *S*-wave velocities, *P*-wave velocities and densities. The starting model is picked randomly from this parameter space. The fit between the modelled and observed dispersion curves is calculated based on an L^2-norm (Wathelet *et al.* 2004), to find the *S*-wave velocity, *P*-wave velocity and density model that best explains the observed dispersion curve. Because surface waves are most sensitive to *S*-wave velocities, we focus the following discussion on the derived *S*-wave velocity model.

If ice and/or firn are isotropic, Rayleigh and Love wave inversion will lead to the same *S*-wave velocity profile. If firn and/or ice are anisotropic, *SH*- and *SV*-wave velocity differ. The dependency of Love waves on *SH*-wave velocity and Rayleigh waves on *SV*-wave velocity will then lead to different inverted *S*-wave velocity profiles.

Inversions were performed separately for the Rayleigh wave observed on the north, and vertical component, for the Love wave on

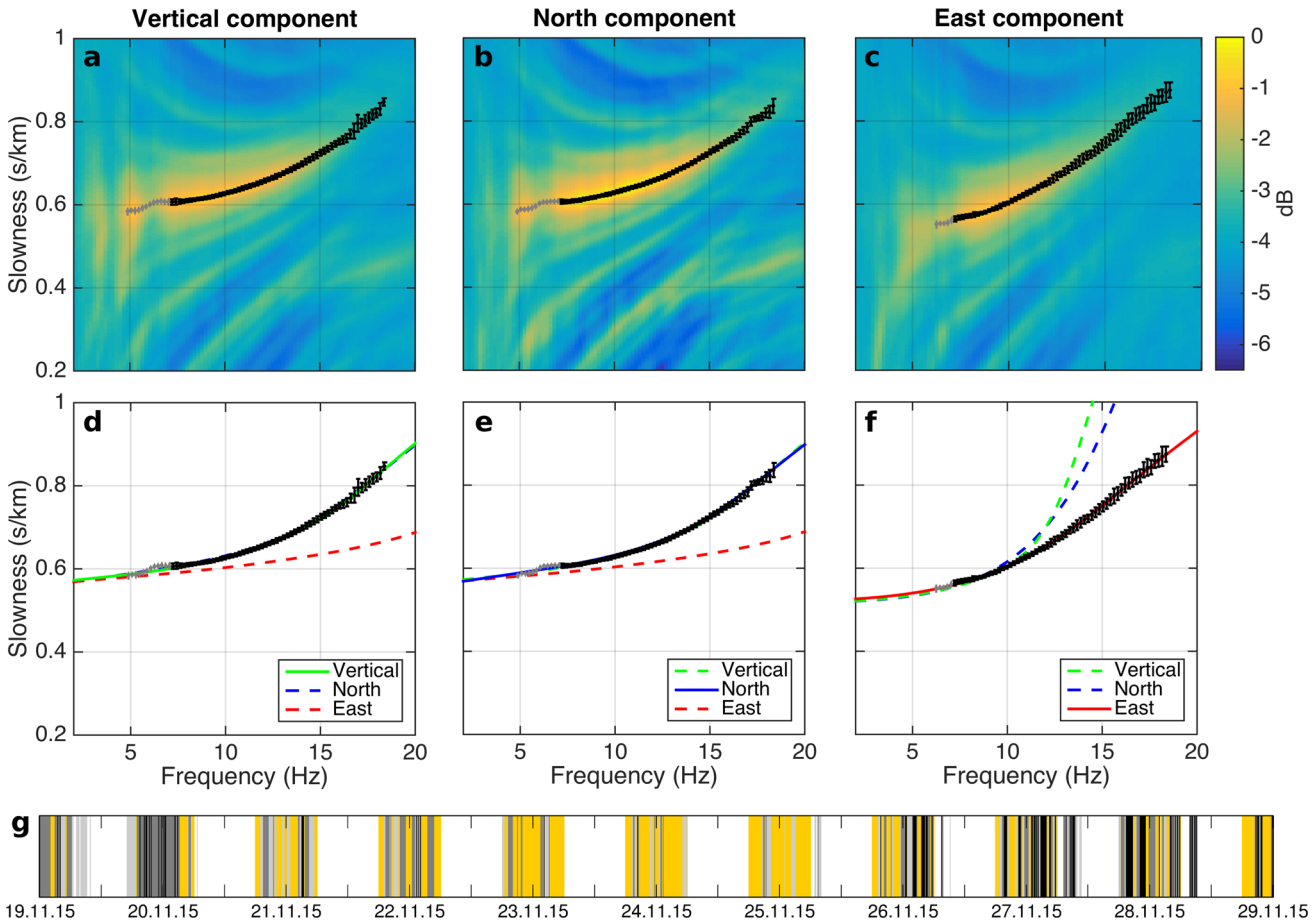

Figure 5. Slowness–frequency space spanning 2–20 Hz, averaged over backazimuth from −20° to 20°, for the (a) vertical, (b) north and (c) east component for distinct dispersion curves between 26 and 28 November. (d–f) Forward modelled dispersion curves (dashed lines) calculated from the results of the different inversions (north, vertical and east component) that gave the lowest misfit (Fig. 6a). The black dots in panels (a)–(f) show the averaged maxima of the fundamental mode dispersion curves that were used for the inversion, with error bars indicating standard deviation. The picked maxima shown with grey dots were not used in the inversions. (g) Occurrence of surface waves over time (UTC) differentiated according to visibility with distinct dispersion curves (black), weaker but still visible dispersion curves (grey) and barley visible dispersion curves (light grey). The yellow blocks show the time between 6:00 and 18:00 at the camp (UTC+12 h).

the east component. The frequency band between 7.2 and 18 Hz used for the inversion is marked by black dots and error bars (Figs 5a–c). Prior to inversion, the dispersion curves were smoothed using five neighbouring frequencies, primarily to reduce dispersion curve variance above 15 Hz.

A parameter space of 16 layers was employed, and the *S*-wave velocity was restricted to 300–2400 m s^{-1}, the *P*-wave velocity to 600–4200 m s^{-1} and the density to 200–910 kg m^{-3} (e.g. Bennett 1968; Kohnen 1972; Albert 1998; Cuffey & Paterson 2010) . An increase in *P*-wave and *S*-wave velocities and density with increasing depth was imposed. A larger parameter space with fewer restrictions resulted in unreasonably low low-velocity layers and overall higher misfits. The inversion depth range was 0–150 m. For each component (Z, N, E), we executed 100 inversions with the above parameterization, finding the model with the best fit for each inversion run. The derived *S*-wave velocity profiles of the 50 best-fit inversions were used to calculate an average *S*-wave velocity profile.

The overall inversion misfits are smallest for the north component and highest for the inversion results from the east component. The velocity–depth profiles for the 50 best-fitting inversion results for each component (misfits between 0.0025 and 0.0066 s km^{-1}) are shown in Fig. 6 (a, thin lines) including the inversion result with the smallest misfit (dashed thick lines). Their averaged velocity–depth profiles are shown in Fig. 6 (a, thick lines) derived from the Rayleigh wave dispersion curve using the north (green) and vertical (blue) components, and the Love wave using the east component (red). We attribute small deviations between the best fitting model and the average model to the large degree of freedom in the inversion process that determines *S*-, *P*-wave velocity, density and depth at the same time.

To illustrate the accuracy of the inverted best fitting *S*-wave velocity profiles (Fig. 6a, dashed thick lines), the corresponding dispersion curves are plotted in Figs 5(d)–(f), solid lines, for example, the solid green line in Fig. 5(d) is the dispersion curve that corresponds to the *S*-wave velocity profile (green dashed line) in Fig. 6(a). Additionally, we used the *S*-wave velocity profile derived from the north (Fig. 6a, blue dashed thick line) and east component (Fig. 6a, red dashed thick line) to forward model Rayleigh wave dispersion curves (Fig. 5d, blue and green dashed lines). Fig. 5(f), shows the same curves in comparison to the picked dispersion curve values of the north component, while Fig. 5(e) shows the equivalent for Love waves in comparison to the picked dispersion curve values of the east component. The calculated Rayleigh wave dispersion curves derived from the north (Figs 5d and e, green), and

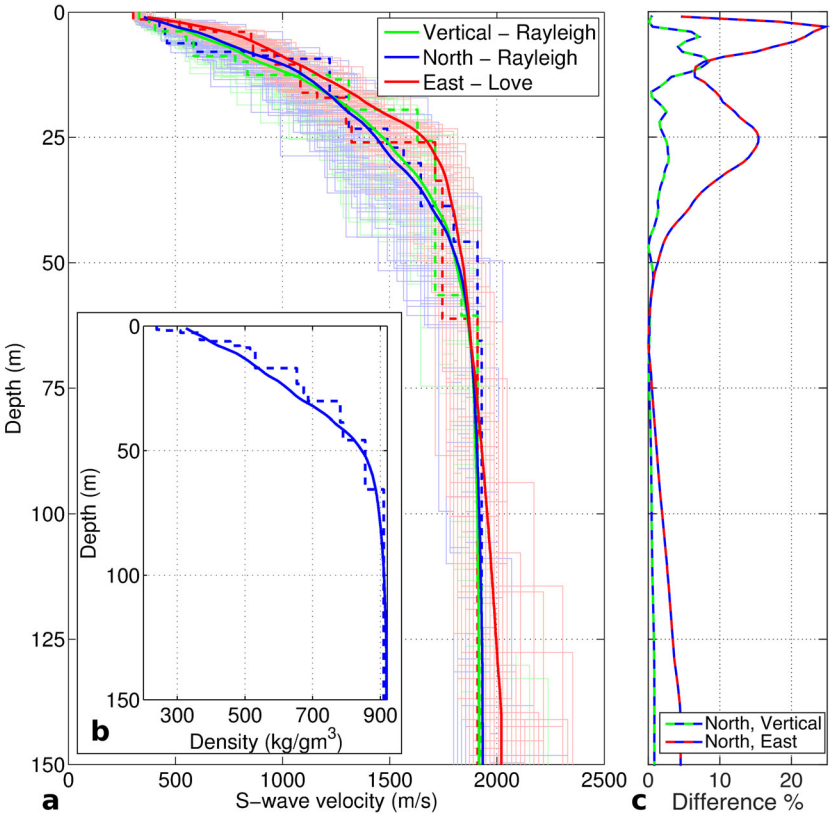

Figure 6. (a) *S*-wave velocity-depth profiles determined from inversion of surface waves (Fig. 5): Rayleigh wave inversion using data from the north (blue) and vertical (green) component; Love wave inversion using data from the east component (red). The 50 inverted profiles fitting the data best are shown as thin lines. The thick solid lines give their average. The profile with the best fit is shown as thick dashed line. (b) Density-depth profile calculated from the *S*-wave velocity–depth profile derived from the north component (blue line in panel a) using the *S*-wave–density relationship given in eq. (2) (solid line). The dashed blue line shows the derived density of the best inversion result (corresponding to panel b dashed blue line). Panel (c) shows the difference between the *S*-wave velocity profile derived from the north and vertical component (green-blue line) and the north and east component (red-blue line), respectively.

the vertical component (Figs 5d and e, blue) are within 1 per cent of the picked frequency–slowness values (Figs 5d and e, black dots), while the Rayleigh wave dispersion curve calculated from the velocity profile of the east component (Love wave) shows slownesses that are constantly too low, up to 21 per cent (Figs 5d and e, red dashed). Similarly, the Love wave dispersion curve (Fig. 5f, red solid) is within 1 per cent of the picked frequency–slowness values (Fig. 5f, black dots), while the Love wave dispersion curves calculated from the velocity profile of the vertical and north components (Rayleigh wave) differ by up to 70 per cent (Fig. 5f, dashed) Hence, the velocity and density profile derived from the Rayleigh wave inversion cannot explain the Love wave dispersion curve, nor can the velocity and density profile derived from the Love wave inversion explain the Rayleigh wave dispersion curve, suggesting anisotropy.

This is reflected in the derived *S*-wave velocity profiles. The averaged *S*-wave velocity–depth profiles (Fig. 6a, thick lines) derived from the dispersion curves of the north and vertical components, that is, from Rayleigh waves, agree within 3 per cent below 12 m (Fig. 6c, green-blue line). Above 12 m they show a difference of up to 8 per cent. The averaged *S*-wave velocity profile derived from the fundamental mode dispersion curve of the east component, that is, from the Love wave, compared to the Rayleigh wave estimate shows up to 24 per cent higher velocities above 12 m and up to 15 per cent higher velocities between 12 and 65 m (Fig. 6c, red-blue line). *S*-wave velocities at 65 m depth are about the same, but show higher velocities of up to 5 per cent for the *S*-wave profile derived from the Love wave inversion below 65 m. Above 12 m, small velocity differences can correspond to large percentage differences due to the slow velocities in the upper few metres. Furthermore, the sensitivity of surface waves to *P*-wave velocity and density can be large at shallow depths (Laske & Widmer-Schnidrig 2007). More important is the observed velocity difference of up to 15 per cent between the *S*-wave velocity profile derived from Rayleigh wave and Love wave dispersion curve between 12 and 65 m (Fig. 6c, red-blue line).

We observe an increase in *S*-wave velocity from 330 m s^{-1} at the surface to 1875 m s^{-1} at 65 m depth. The gradient of velocity increase is stronger for the *S*-wave velocity profile derived from the Love wave (Fig. 6a, red thick line) compared to that derived from the Rayleigh wave (Fig. 6a, blue and green thick line) down to a depth of ∼28 m. Below 28 m the gradient of the velocity increase of the *S*-wave velocity profile derived from the Rayleigh waves is stronger than that derived from the Love wave. The *S*-wave velocity profiles derived from Rayleigh and Love wave inversion nearly reach the same velocity of 1875 m s^{-1} at a depth of 65 m. Hence, the different *S*-wave velocity profiles derived from Rayleigh and Love wave dispersion curve inversions indicate a significant difference of *SV*- and *SH*-wave velocities, that is, seismic anisotropy, which will be discussed in the following section.

4.4 Density–depth profile: seismic anisotropy of firn layer

The firn density increase with depth primarily controls the seismic velocity. The change in density with depth within the firn can thus be obtained from the derived *S*-wave profile (Diez *et al.* 2014). However, inversion of Love and Rayleigh wave dispersion curves resulted in different *S*-wave velocity profiles with the largest differences above 65 m depth, caused by the aforementioned difference in *SH*- and *SV*-wave velocity, that is, seismic anisotropy. Seismic anisotropy within the firn may result from (i) preferred orientation of the hexagonal ice crystals (intrinsic anisotropy), or (ii) thin layers with different velocities, compared to the seismic wavelength (effective or apparent anisotropy), or (iii) a combination of these two effects. Elastic moduli within the firn depend significantly on density and, consequently, so do seismic velocities (Kohnen 1972). High-resolution mm-scale ice-core density measurements show high-density variations within the firn with depth. The variations are up to ± 80 kg m^{-3} at shallow depths, decreasing rapidly within the first 20–30 m (e.g. Freitag *et al.* 2004; Hörhold *et al.* 2011). Density and associated velocity variations on the mm-scale are thin compared to seismic wavelengths of tens of metres in the studied frequency band. This thin layering (layer thickness d) compared to the signal wavelength (λ_w, $d \ll \lambda_w$) results in an effective bulk anisotropy (Backus 1962), reflected in the seismic wave propagation. This should not be confused with the intrinsic anisotropy caused by a preferred orientation of anisotropic crystals (Levshin & Ratnikova 1984; Bodin *et al.* 2015). The layered medium is a vertical transversely isotropic (VTI) medium, that is, anisotropic with a vertical axis of rotation symmetry. In VTI media, *SH*-wave velocities and *SV*-wave velocities are not equal, with their velocity dependent on the angel of incidence. Rayleigh wave velocity, depending on the *SV*-wave velocity, and Love wave velocity, depending on the *SH*-wave velocity, reflect this effective anisotropy.

The north component dispersion curve has the highest energy and the overall smallest misfits. Consequently, the averaged *S*-wave velocity profile derived from the north component is used to derive densities. We estimate the density ρ at depth z using the empirical *S*-wave velocity–density relationship (Diez *et al.* 2014):

$$\rho(z) = \frac{\rho_{\mathrm{ice}}}{1 + [(v_{\mathrm{s,ice}} - v_{\mathrm{s}}(z))/950]^{1.17}}, \tag{2}$$

with ρ_{ice} the density of ice in kg m^{-3}, $v_{\mathrm{s,\,ice}}$ the *S*-wave velocity in ice and v_{s} the *S*-wave velocity at depth z both given in m s^{-1}.

From the derived density–depth profile (Fig. 6b solid blue line) we find the pore close-off, that is, a density of 830 kg m^{-3} where air bubbles form and no air connection to the surface exists any longer (Cuffey & Paterson 2010) at a depth of 47 m. Additionally, we estimate the firn–air content thickness f_{t} from the density profile as

$$f_{\mathrm{t}} = \int_{z=0}^{Z} 1 - \frac{\rho(z)}{\rho_{\mathrm{ice}}} \mathrm{d}z \tag{3}$$

from the surface ($z = 0$) to ice depth (Z) (Fig. 6b, solid blue line) as ∼18 m. This is in good agreement with Kuipers Munneke *et al.* (2014), who modelled firn–air content thickness to be ∼20 m in our region.

5 SURFACE WAVES WITH WATER INTERLAYER

To investigate the influence of the water layer between the ice and sediments on the dispersion curve characteristics, we use the inversion results (Fig. 6) and forward model the firn/ice/water/sediment layered structure using OASES, a seismo-acoustic fast-field algorithm (Schmidt 1988). OASES solves the wave equation for a stratified earth consisting of fluid and solid layers. Fig. 7(j) shows the layer structure of the models studied.

5.1 Forward model: water interlayer

Inputs for the forward model was the best-fit inversion result for the north component (Figs 6a and b, blue dashed line). We use the highest *S*-wave velocity, *P*-wave velocity and density values to extend the ice layer below the inverted depth of 150 m. The dispersion curve of the forward model for a firn layer over a homogenous ice half-space from horizontal, radial particle motion is shown in Fig. 7(a). The frequency-slowness values picked from the north component dispersion curve (Fig. 5b) are overlaid for reference. The fundamental mode (0) between [0 Hz, 0.55 s km^{-1}] and [20 Hz, 0.88 s km^{-1}] and a higher mode (1) between [7 Hz, 0.33 s km^{-1}] and [20 Hz, 0.63 s km^{-1}] are identified.

Next, we introduce a site-appropriate water layer at depths 330 m (Fig. 7b) and 230 m (Fig. 7c), respectively. Introducing a water layer causes the fundamental mode (0) to vanish at a frequency that depends on the overlaying firn/ice thickness. A thinner firn/ice layer gives a higher cut-off frequency. For the 330 m thick firn/ice layer model (Fig. 7b), mode (0) vanishes at 6 Hz compared to 7.5 Hz for the 230 m thick firn/ice overlayer (Fig. 7c). This difference can be explained as (i) the Rayleigh wave sensitivity with depth depends on the wavelength and (ii) the Rayleigh wave particle motion has a shear component that is not supported in water.

We then introduce a seafloor to represent a realistic layered structure of an ice shelf system. The sensitivity of the response to seafloor properties was investigated for dilatant sediments (*P*-wave velocity 1700 m s^{-1}, *S*-wave velocity 200 m s^{-1}, density 1800 kg m^{-3}) and for lithified sediments (*P*-wave velocity 3750 m s^{-1}, *S*-wave velocity 2450 m s^{-1}, density 2450 kg m^{-3}; Peters *et al.* (2008)). The modelled dispersion curve for a homogenous half-space of dilatant sediment below 790 m depth, corresponding to the seafloor depth at the Ross Ice Shelf (Fig. 1c; Albert & Bentley (1990); Fretwell *et al.* (2013)), is shown in Fig. 7(d). A partition of the fundamental mode (0) occurs at 7 Hz. Three branches (Figs 7a–f, labelled 0.1, 0.2 and 0.3) are observed tending towards lower slownesses. This pattern is enhanced with the introduction of a lithified sediment seafloor layer (Fig. 7e). However, the partition occurs at a lower frequency of 6 Hz, and the branches (labelled 0.1, 0.2 and 0.3) have stronger energy. Lastly the firn/ice thickness was reduced for model Fig. 7(f) (equal to that in Fig. 7c), but keeping the water column thickness the same as in Figs 7(d) and (e). For this model the partition of the fundamental mode (0) is observed at 7 Hz and the separation between branches 0.1 and 0.2 increases compared to Fig. 7(e). Hence, the branching of the dispersion curve when a water interlayer is present depends on the thickness of the overlaying firn/ice layer, the thickness of the water column, and the properties of the underlying half-space.

5.2 Comparison of modelled with observed Ross Ice Shelf Rayleigh waves

The observed Rayleigh wave dispersion curves (Figs 5a and b) are in general agreement with the forward modelled dispersion curves (Fig. 7) as the inversion result was used as input to OASES. The main trend of the modelled fundamental mode agrees well with the

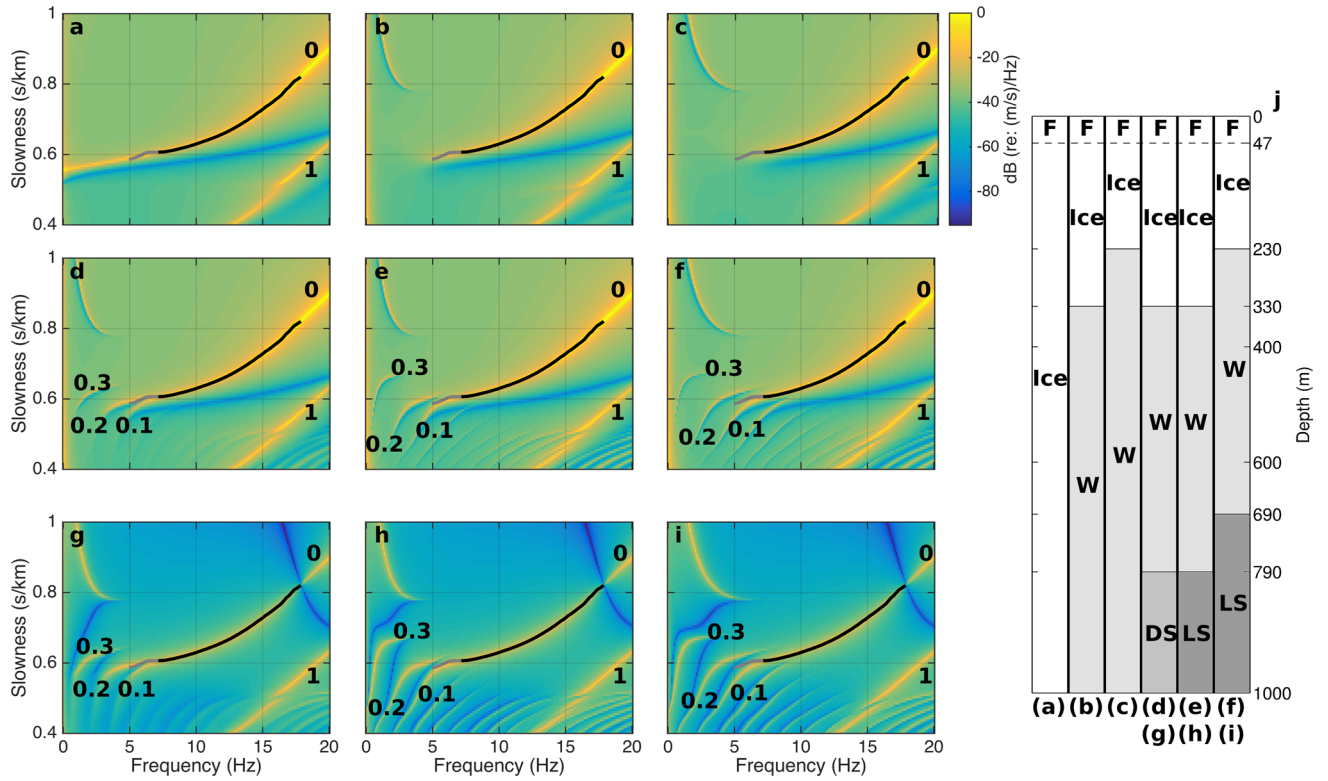

Figure 7. Modelled Rayleigh wave dispersion curves for the horizontal, radial component (a–f) and for the vertical, radial component (g–i) using the velocity (*P*- and *S*-wave) and density profiles having the lowest misfit from the inversion of the north component (Fig. 6a, dashed blue line) for the firn and ice layers. (j) Layer structure used to produce (a)–(i) that includes firn (F), ice (Ice), water (W), dilatant sediment (DS) and lithified sediment (LS) layers. Marked in panels (a)–(i) are the fundamental mode (0), the branches of the fundamental mode (0.1, 0.2, 0.3) and the first higher mode (1). Dilatant sediment (1700 m s^{-1}, 200 m s^{-1}, 1800 kg m^{-3}) and lithified sediment (3750 m s^{-1}, 2450 m s^{-1}, 2450 kg m^{-3}) velocities and densities are from Peters *et al.* (2008). Averaged values of the picked dispersion curve of the north component from Fig. 6(b) are indicated by black and grey line in panels (a)–(i).

observations, that is, the picked Rayleigh wave dispersion curve (black dots). We attribute the decrease in energy at 7.2 Hz for the observed dispersion curves to the influence of the water layer. The higher mode visible in the forward modelled plots (Figs 7a–f, 1) is present to some degree in the observed dispersion curves (Fig. 5b), but the observed higher mode shows lower slownesses (∼0.1 s km^{-1} lower) than the forward modelled curves. However, the higher mode was not used for the inversion, and the difference might be an effect of this *P*-wave velocity model.

A strong peak is visible at ∼5.2 Hz in the Rayleigh wave dispersion curves of the Ross Ice Shelf, with a weaker peak at ∼3.5 Hz. Both span a range of slownesses, decreasing in strength as slowness decreases, and are stronger on the vertical component. Separation into the different branches that are present in the forward modelled data (Figs 7d–f) cannot be identified in the observed dispersion curves. However, this may result from resolution of the SP array data where the two observed peaks may represent different branches.

Frequency-slowness plots for the vertical particle motion (Figs 7g–i) show the same features as the horizontal, radial particle motion (Figs 7d–f). However, the energy of the fundamental mode (0) is higher for the horizontal particle motion. In contrast, for the branches (0.2 and 0.3) after the partition, we observe stronger energies for the vertical particle motion. The overall energy of the Rayleigh wave dispersion curve of the Ross Ice Shelf data (Figs 5a and b) is higher on the north component than on the vertical component, whereas the lower frequency peaks (<7.2 Hz) have higher energy on the vertical component. These differences in energy between north and vertical components are in agreement with the model results, assuming the observed peaks in the Ross Ice Shelf data reflect the fundamental mode branches.

6 SIGNAL ORIGIN

Distinct signals were observed between 0.2 and 0.5 Hz, at 1.6 Hz and above 4 Hz. Polarization analyses in the 0.2–0.5 Hz band and at 1.6 Hz (Fig. 2) show linear polarized waves. The polarization analysis of the DR stations shows that the region of linear polarized waves observed at the SP array between 0.2 and 0.5 Hz extends to lower frequencies (Bromirski *et al.* 2015). The wave propagation and origin of this distinct signal between 0.2 and 0.5 Hz will be resolvable once the year-round data of the BB array is collected. This will allow for beamforming of the lower frequencies (≤2 Hz), due to the larger BB station spacing and improved low-frequency response compared to the SP array.

The signal centred at 1.6 Hz is very narrow-band. Zhan *et al.* (2014) used noise cross-correlation functions of seismometer data from the Amery Ice Shelf and found peaks at 1.5 Hz and multiples thereof, with the vertical component having the strongest energy. They interpret these peaks as resonance frequencies $f_n = n\frac{v_p}{2H}$ (resonance peaks $n = 1, 2, 3, \ldots$) in the water layer of thickness H, that is, a wave repeatedly reflected between the ice shelf bottom and the seafloor. Thus, using the *P*-wave velocity of water

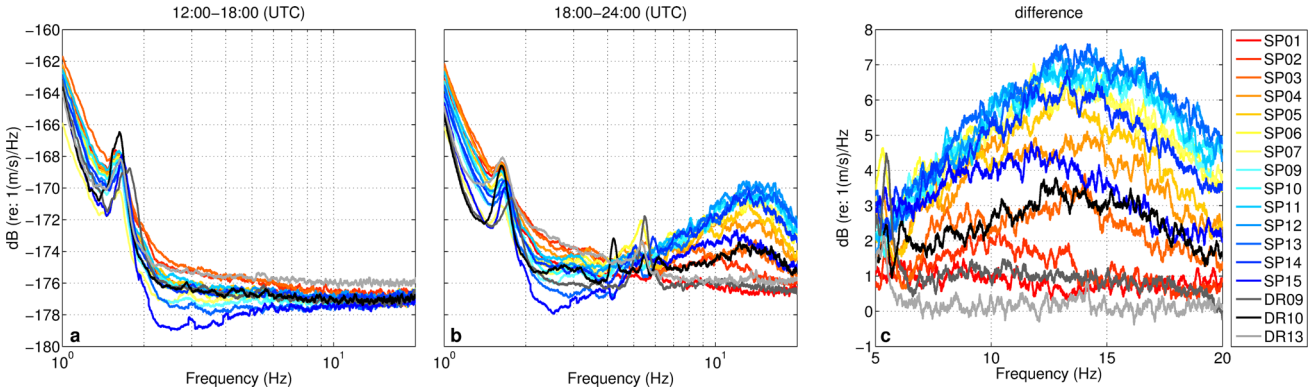

Figure 8. Smoothed spectra of vertical component for SP and BB (DR09, DR10, DR13) stations calculated from 10 min time segments. (a) Spectra for 27 November from 12:00–18:00 (UTC) corresponding to a time when no surface waves were observed (Fig. 5g). (b) Spectra for 27 November from 18:00–24:00 (UTC) corresponding to a time when clear surface waves were observed (Fig. 5g). (c) Difference between (a) and (b) for each station for the frequency band 5–20 Hz.

(v_p = 1500 m s^{-1}), the thickness of the water column can be estimated. Applying this methodology to the noise cross-correlation functions for all the SP stations, we find a prominent peak between 1.61 and 1.62 Hz (not shown). This peak is also visible in the vertical component spectrum for each SP station, as well as in those of the BB stations (Figs 8a and b) between 1.61 and 1.77 Hz, and corresponds to the narrow banded signal at 1.6 Hz in the polarization analysis. Following Zhan *et al.* (2014), we estimate a water column thickness of ∼463 m below DR13 and DR10 and ∼424 m below DR09. This is in good agreement with the RIGGS expedition (Albert & Bentley 1990) water column thickness in this region estimated to be 445 m and the Bedmap2 data (Fretwell *et al.* 2013) water column thickness of 450 m (Fig. 1c).

In addition to beamforming in the frequency domain, classic cross-correlations in the time domain for different frequency bands were performed, showing coherent signals between stations SP01–SP07 and DR10, as well as between stations SP09–SP15, DR10, but weaker correlation with DR09. However, a coherent signal was not found between the SP stations and the station DR13, 7.4 km south of SP01 (Fig. 1), indicating a local source and strong attenuation of the observed surface waves. These signal characteristics are also reflected in the spectra of the different stations (Fig. 8) between 1 and 20 Hz. Fig. 8(a) shows spectra of a time interval without surface waves for comparison with spectra of a time interval with observed surface waves (Fig. 8b). The SP spectra showed higher energy than the DR stations below 4 Hz and lower energy above 4 Hz, likely resulting from different corner frequency signal/noise characteristics, and/or variations in the burial depth of the seismometers. Consequently the SP station spectra were shifted a few dB to allow better comparison. All spectra follow the same trend during the time interval without surface waves (Fig. 8a). The energy for all stations is higher above 5 Hz (Fig. 8b) for the time interval when surface waves are observed, except for station DR13. Fig. 8(c) shows the energy difference between the time interval without (Fig. 8a) and with (Fig. 8b) surface waves. A decrease in energy can be observed above 5 Hz from station SP07 to SP01 (yellow to red), as would be expected for a source from the north. Stations SP09 to SP13 (light to dark blue) all show about the same energy, with weaker energy for station SP14, and even weaker energy for station SP15. The DR10 spectrum (black) shows a clear energy increase. A weak increase in energy (1 dB) is also visible in the spectrum of station DR09.

Three locations are possible for the observed surface waves from the north. First, the surface waves are generated along the shelf front by impact from ocean waves and the waves propagate from the north through the shelf. Second, it is possible that the surface waves are generated locally, for example, due to noise generated from fracturing resulting from movement of the ice shelf by, for example, tides, or due to firnquakes (Lough & Wiens, in preparation). However, it is not clear why these signals should only be produced north of the array and not to the south, east or west, and evidence for highly transient events is not seen except in very limited time windows. Third, another possibility for a locally produced noise is the 'Yesterday' field camp, which was occupied during the entire SP array deployment.

The field camp was located about 2 km north of the corner station SP08. The occurrence of surface wave energy over time (UTC) is shown in Fig. 5(g). Camp operations were at UTC+12 h. Noticeable is the clustering of the occurrence of surfaces wave during McMurdo daytime (Fig. 5g, 6:00–18:00, yellow blocks), when the camp was most active. However, no correlation could be found between the occurrence of surface waves and airplane traffic at the field camp. The observed variations in energy (Fig. 8c) for the different stations suggest a local source. If the ice edge were the source station SP14 and SP15 should have the same energy level as SP09–SP13, since they are about the same distance away from the ice shelf front. The same applies to station DR09 and DR10 that have about the same distance to the ice shelf front. Fig. 8(a) shows that energy levels above 5 Hz are similar for all SP and BB stations, respectively during times without surface waves. Hence, seismometer-ice coupling is not the reason for different energy levels. If the source is the camp, the distances of stations SP09–SP13 to the source are nearly the same ($\leq$1 per cent). Only stations SP14 and SP15 are further away from the camp. Additionally, the distance to DR09 from the camp is 2.7 times as far as that to DR10. Hence, the observed surface wave energy variations suggest a local source in the vicinity of the camp. Combined with the observation of surface waves only during field-camp daytime, we conclude that the source of observed surface waves is indeed the field camp.

7 CONCLUSIONS

We analysed data collected by a three-component small-aperture SP temporary array over an eleven-day period on the Ross Ice Shelf. The most prominent signals observed are Rayleigh and Love wave

arrivals from the north in the 4–18 Hz frequency band. *S*-wave velocity profiles derived from Rayleigh and Love wave inversion differ. We attribute this difference to an effective anisotropy due to thin firn layers with varying densities. The derived firn-air content thickness of 18 m is in good agreement with modelling results (Kuipers Munneke *et al.* 2014).

A spectral peak at about 1.6 Hz identified in the polarization analysis is interpreted as the resonance frequency associated with the thickness of the water layer. The initiation of this wave travelling between ice shelf bottom and seafloor will be investigated in more detail with the year-round data.

The source of the surface wave signal, based on amplitude and temporal variations, is most likely the field camp, possibly generated by snowmobile grooming of the skiway for the planes. Hence, anthropogenic noise produced a seismic signal strong enough to be analysed to infer the firn and ice structure. SP seismic noise from field camps or bases is a well-documented factor affecting the generally quiet noise environment of Antarctica (e.g. Anthony *et al.* 2015). For active-source seismic surveys or other experiments working in this frequency band, the signal-to-noise ratio will likely be substantially improved when such anthropogenic noise is kept to an absolute minimum, that is, carrying out seismic surveys 10 km or more away from occupied stations or camps.

The most striking feature of the dispersion curves is the discontinuous pattern for Rayleigh and Love waves below 7 Hz. We interpret the observed decrease in energy to result from presence of the water layer that is estimated to be about 463 m thick from the spectral peak at ∼1.6 Hz, in agreement with Bedmap2 thickness (Fretwell *et al.* 2013). Love wave dispersion curves do not show an increase in energy below 7 Hz. The Love wave is a pure shear wave, not coupled with a compressional wave like the Rayleigh wave. As the shear modulus is zero in water, Love waves cannot propagate through the water layer and therefore do not exist below the ice-water boundary. However, long wavelength Rayleigh waves can be supported by the complete layer stack of firn, ice, water and seafloor, resulting in a partition of the fundamental mode. Hence, Rayleigh wave dispersion curves, for frequencies associated with wavelengths large enough to reach the seafloor, can be used to resolve ice shelf structure and thickness, water layer thickness and the physical properties of the seafloor.

ACKNOWLEDGEMENTS

PDB, AD and PG were supported by NSF Grant PLR 1246151. RAS was supported by NSF Grant PLR-1246416. DAW, RA and AN were supported under NSF Grants PLR-1142518, 1141916 and 1142126, respectively. PDB also received support from the California Department of Parks and Recreation, Division of Boating and Waterways under contract 11-106-107. We thank Reinhard Flick and Patrick Shore for their support during field work, Tom Bolmer in locating stations and preparing maps and the US Antarctic Program for logistical support. The seismic instruments were provided by the Incorporated Research Institutions for Seismology (IRIS) through the PASSCAL Instrument Center at New Mexico Tech. Data collected are available through the IRIS Data Management Center. The facilities of the IRIS Consortium are supported by the National Science Foundation under Cooperative Agreement EAR-1261681 and the DOE National Nuclear Security Administration. AD thanks Nima Riahi for valuable tips on the processing of passive-source seismic data. We thank Gabi Laske and two anonymous reviewers for their comments and suggestions.

REFERENCES

Albert, D.G., 1998. Theoretical modeling of seismic noise propagation in firn at the South Pole, Antarctica, *Geophys. Res. Lett.,* **25**(23), 4257–4260.

Albert, D.G. & Bentley, C.R., 1990. *Seismic Studies on the Grid Eastern Half of the Ross Ice Shelf: RIGGS III and RIGGS IV,* in *The Ross Ice Shelf: Glaciology and Geophysics*, pp. 87–108, eds Bentley, R.C. & Hayes, D.E., American Geophysical Union.

Anthony, R.E. *et al.*, 2015. The seismic noise environment of Antarctica, *Seismol. Res. Lett.,* **86,** 89–100.

Backus, G.E., 1962. Long-wave elastic anisotropy produced by horizontal layering, *J. geophys. Res.,* **67**(11), 4427–4440.

Banwell, A.F., MacAyeal, D.R. & Sergienko, O.V., 2013. Breakup of the Larsen B Ice Shelf triggered by chain reaction drainage of supraglacial lakes, *Geophys. Res. Lett.,* **40**(22), 5872–5876.

Bassis, J.N., Fricker, H.A., Coleman, R., Bock, Y., Behrens, J., Darnell, D., Okal, M. & Minster, J.-B., 2007. Seismicity and deformation associated with ice-shelf rift propagation, *J. Glaciol.,* **53**(183), 523–536.

Bennett, H.F., 1968. An investigation into velocity anisotropy through measurements of ultrasonic wave velocities in snow and ice cores from Greenland and Antarctica, *PhD thesis,* University of Wisconsin-Madison.

Bentley, C.R., 1990. The Ross Ice Shelf Geophysical and Glaciological Survey (RIGGS): introduction and summary of measurements performed, in *The Ross Ice Shelf: Glaciology and Geophysics*, pp. 1–20, eds Bentley, R.C. & Hayes, D.E., American Geophysical Union.

Bodin, T., Capdeville, Y., Romanowicz, B. & Montagner, J.-P., 2015. Interpreting radial anisotropy in global and regional tomographic models, in *The Earth's Heterogeneous Mantle,* Springer Geophysics, pp. 105–144, eds Khan, A. & Deschamps, F., Springer International Publishing.

Braun, M., Humbert, A. & Moll, A., 2009. Changes of wilkins ice shelf over the past 15 years and inferences on its stability, *The Cryosphere,* **3**(1), 41–56.

Brisbourne, A.M., Smith, A.M., King, E.C., Nicholls, K.W., Holland, P.R. & Makinson, K., 2014. Seabed topography beneath Larsen C Ice Shelf from seismic soundings, *The Cryosphere,* **8**(1), 1–13.

Bromirski, P.D., Sergienko, O.V. & MacAyeal, D.R., 2010. Transoceanic infragravity waves impacting antarctic ice shelves, *Geophys. Res. Lett.,* **37**(2), L02502, doi:10.1029/2009GL041488.

Bromirski, P.D., Diez, A., Gerstoft, P., Stephen, R.A., Bolmer, T., Wiens, D., Aster, R. & Nyblade, N., 2015. Ross ice shelf vibrations, *Geophys. Res. Lett.,* **42,** 7589–7597.

Christianson, K., Jacobel, R.W., Horgan, H.J., Anandakrishnan, S. & Alley, R.B., 2012. Subglacial Lake Whillans — ice-penetrating radar and GPS observations of a shallow active reservoir beneath a west Antarctic ice stream, *Earth planet. Sci. Lett.,* **331–332**(0), 237–245.

Corr, H.F.J., Jenkins, A., Nicholls, K.W. & Doake, C.S.M., 2002. Precise measurement of changes in ice-shelf thickness by phase-sensitive radar to determine basal melt rates, *Geophys. Res. Lett.,* **29**(8), 73-1–74-4.

Cuffey, K.M. & Paterson, W.S.B., 2010. *The Physics of Glaciers,* Elsevier.

Depoorter, M.A., Bamber, J.L., Griggs, J.A., Lenaerts, J.T.M., Ligtenberg, S.R.M., van den Broeke, M.R. & Moholdt, G., 2013. Calving fluxes and basal melt rates of Antarctic ice shelves, *Nature,* **502**(7469), 89–92.

Diez, A., Eisen, O., Weikusat, I., Eichler, J., Hofstede, C., Bohlen, T. & Polom, U., 2014. Influence of crystal anisotropy on seismic velocity analysis, *Ann. Glaciol.,* **55**(67), 97–106.

Drews, R., 2015. Evolution of ice-shelf channels in Antarctic ice shelves, *The Cryosphere Discussions,* **9**(2), 1603–1631.

Dunkin, J.W., 1965. Computation of modal solutions in layered, elastic media at high frequencies, *Bull. seism. Soc. Am.,* **55**(2), 335–358.

Dupont, T.K. & Alley, R.B., 2005. Assessment of the importance of ice-shelf buttressing to ice-sheet flow, *Geophys. Res. Lett.,* **32**(4), L04503, doi:10.1029/2004GL022024.

Eisen, O., Hofstede, C., Diez, A., Kristoffersen, Y., Lambrecht, A., Mayer, C., Blenkner, R. & Hilmarsson, S., 2015. On-ice vibroseis and snowstreamer systems for geoscientific research, *Polar Sci.,* **9**(1), 51–65.

Freitag, J., Wilhelms, F. & Kipfstuhl, S., 2004. Microstructure-dependent densification of polar firn derived from X-ray microtomography, *J. Glaciol.,* **50**(169), 243–250.

Fretwell, P. *et al.*, 2013. Bedmap2: improved ice bed, surface and thickness datasets for Antarctica, *The Cryosphere,* **7**(1), 375–393.

Fricker, H.A., Young, N.W., Coleman, R., Bassis, J.N. & Minster, J.B., 2005. Multi-year monitoring of rift propagation on the amery ice shelf, east antarctica, *Geophys. Res. Lett.,* **32**(2), doi:10.1029/2004GL021036.

Gerstoft, P. & Tanimoto, T., 2007. A year of microseisms in southern california, *Geophys. Res. Lett.,* **34**(20), L20304, doi:10.1029/2007GL031091.

Godio, A. & Rege, R., 2015. The mechanical properties of snow and ice of an alpine glacier inferred by integrating seismic and GPR methods, *J. Appl. Geophys.,* **115**(0), 92–99.

Holland, P.R., Corr, H. F.J., Pritchard, H.D., Vaughan, D.G., Arthern, R.J., Jenkins, A. & Tedesco, M., 2011. The air content of Larsen Ice Shelf, *Geophys. Res. Lett.,* **38**(10), L10503, doi:10.1029/2011GL047245.

Horgan, H.J., Anandakrishnan, S., Jacobel, R.W., Christianson, K., Alley, R.B., Heeszel, D.S., Picotti, S. & Walter, J.I., 2012. Subglacial Lake Whillans–Seismic observations of a shallow active reservoir beneath a West Antarctic ice stream, *Earth planet Sci. Lett.,* **331–332,** 201–209.

Horgan, H.J., Christianson, K., Jacobel, R.W., Anandakrishnan, S. & Alley, R.B., 2013. Sediment deposition at the modern grounding zone of Whillans Ice Stream, West Antarctica, *Geophys. Res. Lett.,* **40**(15), 3934–3939.

Hörhold, M.W., Kipfstuhl, S., Wilhelms, F., Freitag, J. & Frenzel, A., 2011. The densification of layered polar firn, *J. geophys. Res.,* **116**(F1), F01001, doi:10.1029/2009JF001630.

Jansen, D., Luckman, A.J., Cook, A., Bevan, S., Kulessa, B., Hubbard, B. & Holland, P.R., 2015. Brief communication: newly developing rift in Larsen C Ice Shelf presents significant risk to stability, *The Cryosphere,* **9**(3), 1223–1227.

Jurkevics, A., 1988. Polarization analysis of three-component array data, *Bull. seism. Soc. Am.,* **78**(5), 1725–1743.

King, M., Nguyen, L.N., Coleman, R. & Morgan, P., 2000. Strategies for high precision processing of GPS measurements with application to the Amery Ice Shelf, East Antarctica, *GPS Solut.,* **4**(1), 2–12.

Kohnen, H., 1972. Über die Beziehung zwischen Geschwindigkeiten und der Dichte in Firn und Eis, *Zeitschr. f. Geophysik,* **38,** 925–935.

Koper, K. & Hawley, V., 2010. Frequency dependent polarization analysis of ambient seismic noise recorded at a broadband seismometer in the central united states, *Earthq. Sci.,* **23**(5), 439–447.

Kuipers Munneke, P., Ligtenberg, S.R., Van Den Broeke, M.R. & Vaughan, D.G., 2014. Firn air depletion as a precursor of antarctic ice-shelf collapse, *J. Glaciol.,* **60**(220), 205–214.

Laske, G. & Widmer-Schnidrig, R., 2007. 1.03 - theory and observations – normal modes and surface wave measurements, in *Treatise on Geophysics,* pp. 67–125, ed. Schubert, G., Elsevier.

Levshin, A. & Ratnikova, L., 1984. Apparent ansiotropy in inhomogeneous media, *Geophys. J. Int.,* **76**(1), 65–69.

Ligtenberg, S.R.M., Kuipers Munneke, P. & van den Broeke, M.R., 2014. Present and future variations in antarctic firn air content, *The Cryosphere,* **8**(5), 1711–1723.

Liu, Y., Moore, J.C., Cheng, X., Gladstone, R.M., Bassis, J.N., Liu, H., Wen, J. & Hui, F., 2015. Ocean-driven thinning enhances iceberg calving and retreat of Antarctic ice shelves, *Proc. Natl. Acad. Sci. USA,* **112**(11), 3263–3268.

Paolo, F.S., Fricker, H.A. & Padman, L., 2015. Volume loss from antarctic ice shelves is accelerating, *Science,* **348**(6232), 327–331.

Peters, L.E., Anandakrishnan, S., Holland, C.W., Horgan, H.J., Blankenship, D.D. & Voigt, D.E., 2008. Seismic detection of a subglacial lake near the South Pole, Antarctica, *Geophys. Res. Lett.,* **35,** L23501, doi:10.1029/2008GL035704.

Picotti, S., Vuan, A., Carcione, J.M., Horgan, H.J. & Anandakrishnan, S., 2015. Anisotropy and crystalline fabric of Whillans Ice Stream (west Antarctica) inferred from multicomponent seismic data, *J. geophys. Res.,* **120,** 4237–4262.

Pratt, M.J., Winberry, J.P., Wiens, D.A., Anandakrishnan, S. & Alley, R.B., 2014. Seismic and geodetic evidence for grounding-line control of Whillans Ice Stream stick-slip events, *J. geophys. Res.,* **119**(2), 333–348.

Pritchard, H.D., Ligtenberg, S. R.M., Fricker, H.A., Vaughan, D.G., van den Broeke, M.R. & Padman, L., 2012. Antarctic ice-sheet loss driven by basal melting of ice shelves, *Nature,* **484**(7395), 502–505.

Rack, W. & Rott, H., 2004. Pattern of retreat and disintegration of the Larsen B ice shelf, antarctic peninsula, *Ann. Glaciol.,* **39**(1), 505–510.

Riahi, N., Goertz, A., Birkelo, B. & Saenger, E.H., 2013. A statistical strategy for ambient seismic wavefield analysis: investigating correlations to a hydrocarbon reservoir, *Geophys. J. Int.,* **192**(1), 148–162.

Rignot, E., Casassa, G., Gogineni, P., Krabill, W., Rivera, A. & Thomas, R., 2004. Accelerated ice discharge from the antarctic peninsula following the collapse of Larsen B Ice Shelf, *Geophys. Res. Lett.,* **31**(18), L18401, doi:10.1029/2004GL020697.

Rignot, E., Jacobs, S., Mouginot, J. & Scheuchl, B., 2013. Ice-shelf melting around antarctica, *Science,* **341**(6143), 266–270.

Scambos, T., Fricker, H.A., Liu, C.-C., Bohlander, J., Fastook, J., Sargent, A., Massom, R. & Wu, A.-M., 2009. Ice shelf disintegration by plate bending and hydro-fracture: satellite observations and model results of the 2008 wilkins ice shelf break-ups, *Earth planet. Sci. Lett.,* **280**(1–4), 51–60.

Schmidt, H., 1988. Seismo-acoustic fast field algorithm for range independent environments, user's guide, SR 113, SACLANT ASW Research Centre.

Vaughan, D.G., 1994. Investigating tidal flexure on an ice shelf using kinematic GPS, *Ann. Glaciol.,* **20**(1), 372–376.

Vidale, J.E., 1986. Complex polarization analysis of particle motion, *Bull. seism. Soc. Am.,* **76**(5), 1393–1405.

Wathelet, M., 2008. An improved neighborhood algorithm: parameter conditions and dynamic scaling, *Geophys. Res. Lett.,* **35**(9), L09301, doi:10.1029/2008GL033256.

Wathelet, M., Jongmans, D. & Ohrenberger, M., 2004. Surface wave inversion using a direct search algorithm and its application to ambient vibration measurements, *Near Surf. Geophys.,* **2**(4), 211–221.

Zhan, Z., Tsai, V.C., Jackson, J.M. & Helmberger, D., 2014. Ambient noise correlation on the Amery Ice Shelf, east Antarctica, *Geophys. J. Int.,* **196**(3), 1796–1802.